35th Annual International Conference of the IEEE EMBS
Osaka, Japan, 3 - 7 July, 2013

Noninvasive 3D Pressure Calculation From PC-MRI Via Non-Iterative Harmonics-based Orthogonal Projection: Constant Flow Experiment*

MJ Negahdar, Mo Kadbi, J. Cha, J. Cebral, and A. Amini, IEEE Fellow

Abstract— **Use of phase-contrast (PC) MRI in assessment of hemodynamics has significant clinical importance.**

In this paper we develop a novel approach to determination of hemodynamic pressures. 3D gradients of pressure obtained from Navier-Stokes equation are expanded into a series of orthogonal basis functions, and are subsequently projected onto an integrable subspace. Before the projection step however, a scheme is devised to eliminate the discontinuity at the vessel and image boundaries. In terms of the computation time, the proposed approach significantly improves on previous iterative methods for pressure calculations.

The method has been validated using computational fluid dynamic simulations and in-vitro MRI studies of stenotic flows.

1. Introduction

Phase contrast MRI is widely used to noninvasively measure blood velocity and flow in vivo [1]. PC-MRI can derive all three velocity components within a 3D imaged volume. The velocity field can then be used to obtain flow pattern wall shear stress, vascular compliance, blood pressure, and other hemodynamic information.

Noninvasive calculation of the relative pressure field within the cardiovascular system has received significant attention in recent times. Relative pressure drop across a stenotic narrowing provides an important indication regarding the hemodynamic severity of a stenosis and is a significant physiologic parameter in planning a revascularization. Based on fluid mechanics of Newtonian and incompressible flow, pressure gradients can be derived from the 3-D velocity field by using the Navier-Stokes equation [2, 11]. Song [3] introduced an iterative solution to the pressure-Poisson equation for deriving pressure fields from Ultrafast CT cardiac images. Later, this method was extended and adopted to derivation of pressures from PC MRI by [2-4, 7-9]. Ebbers et al. [5] also presented a method to integrate pressure gradient (obtained from Navier-Stokes) but along user defined lines placed within a 3D phase contrast MRI dataset. In [7], the authors proposed a new solver to improve computation of cardiovascular relative pressure field using a multi-grid based solver with Galerkin coarsening. Wang et al. [6] proposed a new method for obtaining relative pressure maps using non-iterative harmonic based algorithm. A significant limitation of the method however was that it was only applicable to 2D PC MRI in 2-D axi-symmetric coordinates. In this paper, we significantly improve on [6] by extending the framework to 3D PC MRI and 3D coordinates. Reformulation of the method from axis-symmetric to general non-axi-symmetric coordinates makes the method applicable to a variety of cases including in-vivo data.

* This work was supported in part by the National Science Foundation under Grant 0730467 and by an innovative grant from the Clinical and Translational Research Program of the University of Louisville to A. Amini

MJ Negahdar, M. Kadbi and J. Cha are with the Medical Imaging Lab, Dept. of Electrical & Computer Engineering, University of Louisville. Louisville, KY 40292 USA. Phone: 502-852-3400; fax:502-852-1577 (e-mail: m0nega02@exchange.louisville.edu).

J. Cebral is professor of Department of Computational and Data Sciences George Mason University. Fairfax, Virginia 22030

A. A. Amini is Professor of Electrical and Computer Engineering and Endowed Chair in Bioimaging at University of Louisville. Louisville, KY

2. Materials and Methods

Navier-Stokes equation, the law of conservation of momentum, governs motion of Newtonian fluids. If we assume that viscosity is constant, Navier-Stokes equation can be written as:

$$\widehat{\nabla P} = -\rho \frac{\partial \boldsymbol{u}}{\partial t} - \rho(\boldsymbol{u}.\nabla)\boldsymbol{u} + \mu\nabla^2\boldsymbol{u} + \rho f \qquad (1)$$

where u(x,y,z,t) is the fluid vector velocity from PC MRI , P is the scalar pressure, ρ is the density of the fluid and f is the body force. Generally in closed systems, the body forces are negligible and can be ignored.

Due to the noise in PC-MRI velocity data, the pressure gradient field $\widehat{\nabla P} = (\hat{P}_x, \hat{P}_y, \hat{P}_z)$ is not curl-free, and therefore it cannot be the true gradient of the scalar pressure field. An extremum principle is cast to find P such that ∇P is the projection of $\widehat{\nabla P}$ onto the curl-free subspace of integrable vector fields.

2.1. Non-Iterative Harmonic-Based Orthogonal Projection

The integrability condition requires:

$$\frac{\partial P_x}{\partial z} = \frac{\partial P_z}{\partial x}, \frac{\partial P_y}{\partial z} = \frac{\partial P_z}{\partial y}, \frac{\partial P_x}{\partial y} = \frac{\partial P_y}{\partial x} \qquad (2)$$

The projection of $\widehat{\nabla P}(x,y,z) = (\hat{P}_x, \hat{P}_y, \hat{P}_z)$ onto an integrable subspace would then involve minimizing the following energy function:

$$D = \iint_\Omega \left|\tilde{P}_x - \hat{P}_x\right|^2 + \left|\tilde{P}_y - \hat{P}_y\right|^2 + \left|\tilde{P}_z - \hat{P}_z\right|^2 \, dxdydz \qquad (3)$$

The conventional approach [2-4,7-9], to minimizing D, involves derivation of the Euler-Lagrange equation which in this case is the pressure-Poisson equation, which is then iteratively solved subject to natural boundary conditions. In lieu of the iterative approach, and provided a series of orthogonal integrable basis function $\phi(x,y,z,\bar{\omega})$ with $\bar{\omega}$ as the vector $(\omega_x, \omega_y, \omega_z)$ of spatial frequencies, the pressure $\tilde{P}$ can be expanded as:

$$\tilde{P} = \sum \tilde{C}(\bar{\omega}) \, \phi(x,y,z,\omega) \qquad (4)$$

Its gradients will have $\widetilde{P_l} = \sum \tilde{C}(\bar{\omega}) \, \phi_l(x,y,z,\omega)$, with $\phi_l = \frac{\partial \phi}{\partial l}$ and $l = x,y,z$. The measured gradient can also be expanded as

$$\widehat{P_l} = \sum \widehat{C_l}(\varpi)\ \phi_l(x, y, z, \omega) \quad (5)$$

Following Frankot and chellappa [10], the coefficient of expansion of the projected pressure $\widetilde{P}$ in the integrable subspace, is related to $\widehat{C_x}$, $\widehat{C_y}$, and $\widehat{C_z}$ by:

$$\widetilde{C} = \frac{\widehat{C_x} T_x + \widehat{C_y} T_y + \widehat{C_z} T_z}{T_x + T_y + T_z} \quad (6)$$

Where $T_l = \int_{\mathbb{R}^3} |\phi_l|^2\ dx\ dy\ dz$. Therefore, by substituting $\widetilde{C}(\varpi)$ from equation (6) into equation (4), integrable pressure gradients and the correctly integrated pressure field will easily be obtained. Note that the pressure field is reconstructed in one-pass (with no iterations) using all of the available information in $\widehat{P_x}$, $\widehat{P_y}$ and $\widehat{P_z}$. In this paper, Fourier basis functions are adopted for $\phi(\varpi)$ for convenience of computation using the fast Fourier Transform (FFT).

The key differences between Frankot and Chellapa's method [10] (which is about reconstructing surface shape from shading information) and our method are: (i) Since FFT needs to be applied to a 3D cubical domain, while PC velocity information is only available within the vessel lumen, the PC data needs to be extrapolated at the boundaries in order to remove discontinuities and (ii) FFT assumes that the data is periodic and, therefore, a discontinuity in the periodic extension of pressures will exist which once again needs to be removed.

2.2 Data Extrapolation

The projection of pressure gradient using Fourier transform does not work in presence of discontinuities. There are two kinds of discontinuities which affect the projections. First, is discontinuity at vessel or phantom walls. Vessel lumen does not cover the entire image domain; however, the whole of the image domain will be "projected" by this method. Second, a discontinuity exists at the image boundary since Fourier transform assumes that the data is periodic and a discontinuity in the periodic extension of data will exist. Figure (1) shows a schematic of vessel wall with vessel and image boundary discontinuities at r_b and r_L respectively.

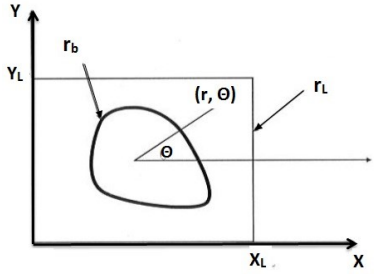

Figure 1. Illustration of the discontinuity problem at boundaries. The figure in bold illustrates a slice of physical vessel or flow phantom with $0 < r < r_b(\theta)$ at a fixed z and r_L indicates imaging boundaries.

To eliminate pressure discontinuity at vessel boundaries, first we transform each slice into the polar coordinate system, and we subsequently perform the following pressure assignment on empty space to keep pressure profile smooth and continuous along radial directions.

$$\hat{P}(r,\theta) = \begin{cases} \hat{P}(r_b,\theta) & if \quad r_b(\theta) < r < r_L(\theta) \\ \hat{P}(r,\theta) & if \quad r < r_b(\theta) \end{cases} \quad (7)$$

Following the assignment, polar coordinate is transformed back to the Cartesian coordinate system. To keep continuity in the periodic extension, in Cartesian coordinates, a symmetric extension of pressure can be adopted:

$$\hat{P}(x,y,z) = \hat{P}(x,y,-z) = \hat{P}(x,-y,z) = \hat{P}(-x,y,z) = \hat{P}(-x,-y,z) = \hat{P}(x,-y,-z) = \hat{P}(-x,y,-z) = \hat{P}(-x,-y,-z) \quad (8)$$

If we assume imaging dimension $[0\sim X_L, 0\sim Y_L, 0\sim Z_L]$, after applying the above extension, new image dimensions will be $[-X_L\sim X_L, -Y_L\sim Y_L, -Z_L\sim Z_L]$ which is 8 times bigger than original image dimensions. Figure 2 demonstrates components of the pressure gradient in the x direction before and after applying the above extensions in an axial slice proximal to stenosis. Through adoption of the stated approach in this section, discontinuities both at the vessel and image boundaries will be removed. We note that no claim is made here that this is the best or most optimal approach to removal of discontinuities. However, the adopted approach is straight forward and fast.

2.3. Flow Circuit

Experiments were carried out using a closed loop flow system Figure (3). A MR compatible, computer controlled pump (CardioFlow 1000 programmable pump Shelley Medical Imaging Technologies, London, Ontario, Canada) with the capability to generate user-provided flow waveforms was used. An idealized rigid model of axisymmetric Gaussian shape was machined from transparent acrylic using conventional CNC machining methods initially aimed at 90% area occlusion. Later, the exact geometry was measured with high-resolution CT scans (0.22 × 0.22 × 0.625 mm3) and the area occlusion was found to be 87%. There were additional imperfections in fabrication of the phantom which caused the phantom geometry to not be completely axi-symmetric.

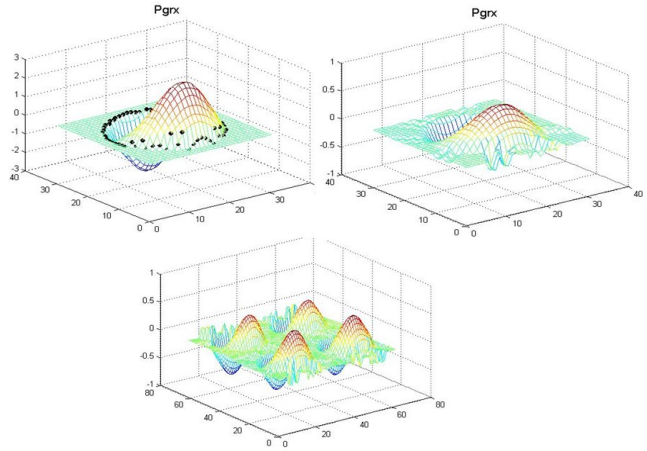

Figure 2. Top-left: Pressure gradients in x direction obtained from Navier-Stokes equations shown for one axial slice in the stenotic phantom, black dots indicates boundary points. Top-right: Extrapolated pressure gradients outside of phantom boundary (equation (7)). Bottom: Resulting pressure gradients after data extrapolation in order to remove discontinuities at image boundaries. Data replication is according to equation (8).

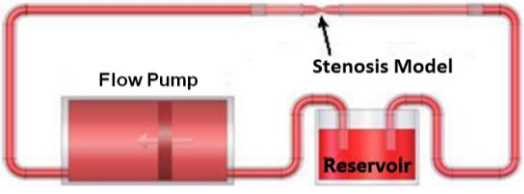

Figure 3. Schematic of the stenotic flow circuit used in MRI experiments. Within the phantom, flow goes from left to right. Note that the z coordinate runs along the phantom and x,y coordinates are axial to the phantom.

The stenosis diameter narrowed from 25.4 mm at the inlet to 9.04 mm at the throat. To ensure fully developed laminar flow at the entrance of the model, a 75-cm long straight rigid acrylic tube was placed upstream of the test section. The viscosity of the blood- mimicking solution utilized in the flow circuit was measured using a LVT Cone-Plate viscometer (Brookfield Labs., Stoughton, MA, USA) to be 0.0043 Pa.s at 68°F. The density of the solution was 1035 kg/m3.

2.4. MRI Experiments

Two separate flow rates were considered for the MRI experiments. In the first case, a flow rate of 13.2 ml/sec was used which corresponds to a Reynolds number (Re) [11] of 160 which is encountered in the iliac artery. In the second case, a flow rate of 39.6 ml/sec was used. For our phantom, this flow rate corresponds to a Reynolds numbers of 480 and is the mean Reynolds number encountered in the in Carotids. Stenosis in these two arteries has a significant importance in clinical applications.

Imaging was performed on a Philips Achieva 1.5T scanner (Philips Healthcare, Best, NL). To measure the velocity, a multi-slice 2D turbo gradient echo sequence was utilized that included a bipolar velocity encoding gradient in a single predetermined direction. Conventional Cartesian trajectory was chosen for image acquisition. The remaining sequence parameters were as follows: FOV = 96x96 mm, 1.5x1.5 mm acquired in-plane resolution, 4 mm slice thickness, flip angle = 5, matrix size = 64x64, TR/TE = 7.6/4.4 ms (for Reynolds number 480) and 8.0/5.0 ms (for Reynolds number 160). In order to ensure good signal quality, an 8-element phased-array knee coil was used. The phantom was placed at the center of the knee coil and images were acquired at or as close to the iso-center of the magnet as possible. With the z = 0 location corresponding to the center of the stenosis, axial slices were collected at locations both proximal and distal to the stenosis.

2.5. CFD Simulations

Computational Fluid Dynamic (CFD) simulations were carried out for two steady flow experiments using previously developed software [12]. For this purpose, the geometrical model of the 87% area occluded phantom was reconstructed from high-resolution CT (resolution 0.22 × 0.22 × 0.625 mm3) and finite element grids with sufficient resolutions were generated. Five points were placed within the boundary layer region close to the walls. The computational grid contained about 8 million tetrahedral elements. Subsequently, the 3D unsteady Navier-Stokes equations were numerically solved using a finite element formulation. Since flows can become unsteady even for steady inflow conditions, the Navier-Stokes equation was solved using a time accurate explicit integration scheme. A fully developed parabolic velocity profile was prescribed at the model inlet and traction-free boundary conditions were applied at the outlet boundary. Figure 4 shows the velocity fields on mid-saggital plane of 87% area stenosis phantom for the two MRI experiments (Re=160 and Re =480).

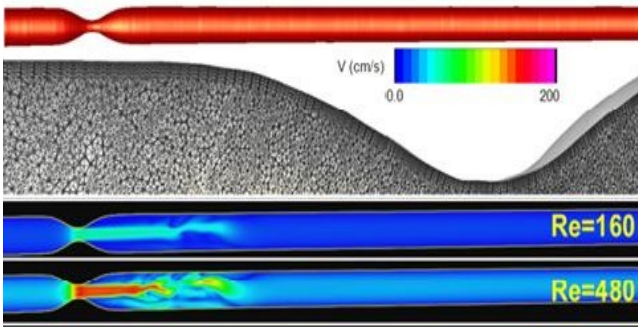

Figure 4. Steady flow simulations in the 87% stenosis phantom. Top: Geometry constructed from high resolution X-ray CT data. Middle: Details of computational grid on middle plane (observe boundary layer gridding). Bottom: Magnitude of velocities on mid-sagittal plane for different Reynolds numbers Re=160 and Re=480.

3. RESULTS

Two types of comparisons were made: in one instance, the pressures derived from noise-corrupted CFD velocities using both the new 3D non-iterative pressure calculation technique as well as the iterative solution to pressure-poisson equation were compared with CFD simulated pressures. In a second instance, the pressures derived from in-vitro MRI studies were compared with CFD velocities. In adding noise to CFD-simulated velocities, Gaussian distributed noise with zero mean and standard deviation of σ was used. Figure 5 shows CFD generated pressures (red line), the pressures calculated by the 3D iterative method (blue dotted line) and the pressures calculated by the 3D non-iterative method (black dotted line) for Reynolds number of 160 (left column) and Reynolds number of 480 (right column) for the case of $\sigma = 0.08$

Table 1 reports the relative error (R.E.) (equation (9)) in computing the pressure drop (PD) between the calculated pressures and CFD simulated pressures for a range of standard deviation for noise. As can be seen in table1, Harmonic based method is a bit more sensitive to noise power rather than iterative method, however results are all in acceptable range.

$$\text{R. E.} = \frac{\text{PD}_c - \text{PD}_{\text{CFD}}}{\text{PD}_{\text{CFD}}} * 100\ \% \qquad (9)$$

To compare pressure calculation from CFD simulation to those from MRI experiments, CFD data were regridded to MRI resolution on a Cartesian uniform grid. Figure 6 shows comparison between 3D CFD simulated pressures and 3D calculated pressures by iterative and non-iterative techniques for Reynolds numbers of 160 and 480.

As may be seen, the iterative method slightly underestimates the pressures relative to the non-iterative method. It should also be noted that due to pump imperfections and distal resistance in flow circuit as well as PC-MRI noise, the flow rates calculated at each cross section inside the phantom was 12% smaller than the programmed flow rates. Therefore, in reality, we expect the pressure drops from both the iterative and non-iterative techniques to have a smaller discrepancy with the CFD simulated pressures than what has been shown.

Finally, for the in-vitro studies described here, the computational time for obtaining the relative pressures was 4.83 seconds on a quad core 2.4 GHz CPU processor with 8GB of memory for deriving the 3D pressure field from 50

axial PC MRI slices. This is to be compared with 87.4 seconds for the iterative approach on the same platform.

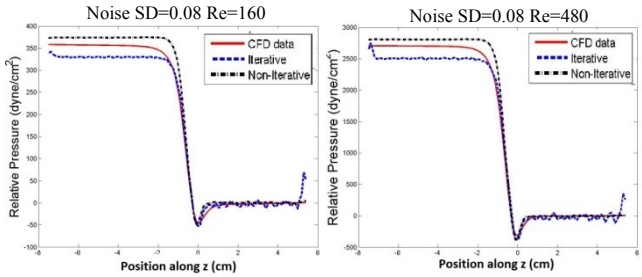

Figure 5. Comparison of CFD generated pressures (red line) with those calculated with 3D non-iterative harmonic-based orthogonal projection (black dotted) and iterative solution to Pressure-Poisson equation (blue dotted line) using noise corrupted CFD simulated velocities at Re=160 (left column) and Re=480 (right column). In both cases, additive Gaussian noise with σ=0.08 was added to the 3D CFD simulated velocity fields. Please note that only pressure along the centerline of the phantom is displayed. Also, note that the zero position is the center of the phantom with positive coordinates corresponding to flow distal to the stenosis and negative coordinates corresponding to flow proximal to the stenosis.

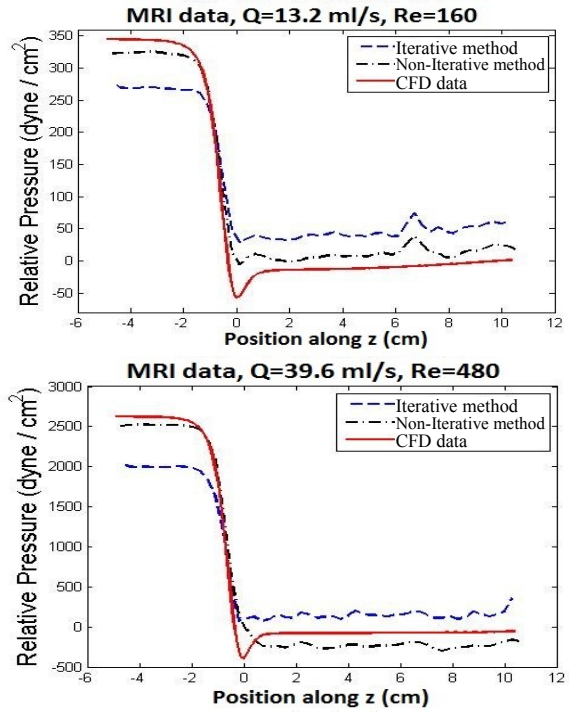

Figure 6. Comparison of CFD simulated pressures (red line) with those calculated with the iterative method (black dotted line) and non-iterative method (Blue dotted line) using in-vitro PC-MRI data for constant flows with Reynolds numbers Re = 160 (top) and Re = 480 (bottom). Please note that only pressure along the centerline of the phantom has been displayed.

	σ	0.00	0.02	0.04	0.06	0.08
Flow Regime	**Method**	**R.E.**				
Re=160	Iterative	8 %	7 %	6 %	8 %	2 %
	Non-iterative	12 %	11 %	7 %	0 %	3 %
Re=480	Iterative	7 %	7 %	9 %	8 %	4 %
	Non-iterative	14 %	13 %	10 %	5 %	2 %

Table1. Relative error (R.E.) in comparing the pressure drop between the calculated and CFD simulated pressures for both iterative and non-iterative methods for Reynolds number 160 and 480.

4. CONCLUSIONS

In In this paper, we have introduced a new 3D non-iterative method which results in significant computational savings for calculation of intravascular pressures from phase-contrast MRI while providing good accuracy. The approach involves expanding the pressure gradient with a series of orthogonal basis functions and subsequently projecting them onto an integrable subspace in order to calculate the 3D relative pressure maps. Results from simulations and in-vitro phantom studies showed good agreement between the new method and the conventional iterative method and pressure maps directly generated by CFD.As demonstrated, when using Fourier basis functions, the algorithm applies three 3D FFT's and one inverse 3D FFT to arrive at the results.

Future work will involve application of the method on pulsatile stenotic flows in phantom experiments as well as in patients with atherosclerotic disease.

REFERENCES

[1] N. J. Pelc, S. FG, B. T. Li KC, H. RJ and E. DR, "Quantitative magnetic resonance flow imaging," *Magn Reson Q,* vol. 10, pp. 125-47, Sep 1994.

[2] G.-Z. Yang, P. J. Kilner, N. B. Wood, S. R. Underwood and D. N. Firmin, "Computation of flow pressure fields from magnetic resonance velocity mapping," *Magnetic Resonance in Medicine*, vol. 36, pp. 520-526, 1996.

[3] S. M. Song, R. M. Leahy, D. P. Boyd, B. H. Brundage and S. Napel, "Determining cardiac velocity fields and intraventricular pressure distribution from a sequence of ultrafast CT cardiac images," *IEEE Transactions on Medical Imaging,* vol. 13, pp. 386-397, 1994.

[4] J. M. Tyszka, D. H. Laidlaw, J. W. Asa and J. M. Silverman, "Three-dimensional, time-resolved (4D) relative pressure mapping using magnetic resonance imaging," *Journal of Magnetic Resonance Imaging,* vol. 12, pp. 321-329, 2000.

[5] T. Ebbers, L. Wigström, A. F. Bolger, J. Engvall and M. Karlsson, "Estimation of relative cardiovascular pressures using time-resolved three-dimensional phase contrast MRI," *Magnetic Resonance in Medicine,* vol. 45, pp. 872-879, 2001.

[6] Y. Wang, A. N. Moghaddam, G. Behrens, N. Fatouraee, J. Cebral, E. T. Choi, and A. A. Amini ,"Pulsatile Pressure Measurement Via Harmonic-Based Orthogonal Projection of Noisy Pressure Gradients," proceedings of SPIE Medical Imaging Conference on Physiology, Function, and Structure from Medical Images, San Diego, California, February 2006

[7] T. Ebbers and G. Farnebäck, "Improving computation of cardiovascular relative pressure fields from velocity MRI," *Journal of Magnetic Resonance Imaging*, vol. 30, pp. 54-61, 2009.

[8] J. Bock, A. Frydrychowicz, R. Lorenz, D. Hirtler, A. J. Barker, K. M. Johnson, R. Arnold, H. Burkhardt, J. Hennig and M. Markl., "In vivo noninvasive 4D pressure difference mapping in the human aorta: Phantom comparison and application in healthy volunteers and patients," *Magnetic Resonance in Medicine,* vol. 66, pp. 1079-1088, 2011.

[9] A. Nasiraei-Moghaddam, G. Behrens, N. Fatouraee, R. Agarwal, E. T. Choi and A. A. Amini, "Factors affecting the accuracy of pressure measurements in vascular stenoses from phase-contrast MRI," *Magnetic Resonance in Medicine,* vol. 52, pp. 300-309, 2004.

[10] R. T. Frankot and R. Chellappa, "A method for enforcing integrability in shape from shading algorithms," IEEE Transactions on Pattern Analysis and Machine Intelligence, vol. 10, pp. 439-451, 1988.

[11] M. C. Potter and J. F. Foss, Fluid Mechanics, Great Lakes Press, Okemos, MI, 1982..

[12] J. R. Cebral, M. A. Castro, S. Appanaboyina, C. Putman, D. Millan, A. Frangi, "Efficient pipeline for image-based patient-specific analysis of cerebral aneurysm hemodynamics: technique and sensitivity." *IEEE Transactions on Medical Imaging, vol.* 24, no. 4, pp. 457-467, 2005.